Room-Temperature Transport of Indirect Excitons in (Al,Ga)N/GaN Quantum Wells

F. Fedichkin,[1] T. Guillet,[1] P. Valvin,[1] B. Jouault,[1] C. Brimont,[1] T. Bretagnon,[1] L. Lahourcade,[2] N. Grandjean,[2] P. Lefebvre,[1] and M. Vladimirova[1,*]

[1]*Laboratoire Charles Coulomb, UMR 5221 CNRS-Université de Montpellier, 34095 Montpellier, France*
[2]*Institute of Physics, EPFL, CH-1015 Lausanne, Switzerland*

(Received 3 March 2016; revised manuscript received 30 May 2016; published 20 July 2016)

We report on the exciton propagation in polar (Al, Ga)N/GaN quantum wells over several micrometers and up to room temperature. The key ingredient to achieve this result is the crystalline quality of GaN quantum wells grown on GaN substrate that limits nonradiative recombination. From the comparison of the spatial and temporal dynamics of photoluminescence, we conclude that the propagation of excitons under continuous-wave excitation is assisted by efficient screening of the in-plane disorder. Modeling within drift-diffusion formalism corroborates this conclusion and suggests that exciton propagation is still limited by the exciton scattering on defects rather than by exciton-exciton scattering so that improving interface quality can boost exciton transport further. Our results pave the way towards room-temperature excitonic devices based on gate-controlled exciton transport in wide-band-gap polar heterostructures.

DOI: 10.1103/PhysRevApplied.6.014011

I. INTRODUCTION

An indirect exciton (IX) in a semiconductor quantum well (QW) is a quasiparticle composed of an electron and a hole separated along the growth direction but still bound by Coulomb interaction. IXs can be realized in both wide single QWs [1] and in coupled QWs [2]. The prominent feature of IXs is their long lifetime, exceeding lifetimes of regular direct excitons by orders of magnitude [3,4]. Their long lifetimes allow IXs to travel over large distances before recombination, providing the opportunity to study exciton transport by optical imaging [5–7]. Moreover, they possess strong permanent dipole moments along the growth axis, which is essential for electrical control of excitonic fluxes and for excitonic device operation [7–11]. Various device schemes based on IXs have been implemented, such as excitonic light storage devices [12], exciton optoelectronic transistors [9], all-optical excitonic transistors [10,11], excitonic integrated circuits [13], and integrated exciton multiplexers [14]. Device architectures based on topological properties of the excitonic states have been recently proposed [15]. For optical signal processing, the advantage of excitons is that they effectively convert photons to dimensions that are compatible with electronics. Excitons are neutral particles, potentially allowing excitonic devices to operate without the resistive-capacitive delays that retard conventional electronics. The interconnects and switches that rely on excitons combining the advantageous data-processing speed of photons with the integration densities of modern electronics may constitute a promising future technology that bridges electronics and optics in a single device [16].

IXs were most extensively studied in GaAs-based QWs [2,5,17–21], but recently their realization in wide-band-gap semiconductors such as GaN [22] and ZnO [23] has been considered. GaN/(Al, Ga)N and ZnO/(Zn, Mg)O wide QWs grown along the (0001) crystal axis naturally exhibit built-in electric fields up to megavolts per centimeter [24,25] so that IXs are naturally created in the absence of any external electric field. Such IXs have binding energies of tens of millielectroinvolts, largely above the 4 meV reached in a typical GaAs-based structure [26,27]. This robustness may extend the operation of the excitonic devices up to room temperature. Furthermore, such materials are promising candidates for the realization of coherent states of IXs at temperatures higher than a fraction of kelvin [28,29]. These properties make materials with robust IXs particularly interesting. Nevertheless, so far, even in these materials with robust excitons, there was no evidence of room-temperature transport [22,23]. Indeed, there is a number of obstacles to be overcome or bypassed in order to demonstrate room-temperature transport in QWs based on polar wide-band-gap semiconductors including (i) dramatic dependence of exciton radiative lifetime on the exciton density that makes exciton density measurement more complex than in conventional GaAs-based structures [30], (ii) thermally activated nonradiative recombination that quenches exciton PL at room temperature [31], (iii) coexistence of photon propagation with exciton propagation along the QW plane [22], and (iv) strong inhomogeneous broadening of the exciton emission due to both monolayer fluctuations of the QW thickness and the fluctuations of alloy composition in the barriers [32].

In this paper, we address all these issues and demonstrate excitonic transport up to room temperature over distances up to 5–10 μm in a GaN/(Al, Ga)N QW grown on GaN

*maria.vladimirova@umontpellier.fr

free-standing (FS) substrate. By comparing time-resolved photoluminescence (PL) and spatially resolved microphotoluminescence (μPL) images of two identical QWs grown, respectively, on GaN and on sapphire, we reveal the important role played by substrates in exciton propagation. First, the radiative efficiency appears to be higher for GaN-grown structures, with much weaker temperature-induced quenching due to lower threading dislocation densities [33]. Second, the absence of dielectric mismatch between the substrate and the epilayer strongly limits the photon-guiding effect along the plane of the structure, making exciton transport easier to distinguish from photon propagation [22]. Careful benchmarking of spatial and temporal dynamics suggests that even in the best-quality QWs grown on GaN FS substrates, most exciton propagation in the optically excited QW takes place in the regime where built-in electric field is efficiently screened by the presence of relatively high densities of IXs. Modeling of the exciton expansion within the drift-diffusion formalism allows us to conclude that the propagation is still limited by the exciton scattering on pointlike defects rather than by exciton-exciton scattering so that improving interface quality can boost exciton transport further. These results constitute an important building block for our understanding of exciton transport in wide-band-gap polar heterostructures and pave the way towards room-temperature excitonic devices.

II. SAMPLES AND EXPERIMENTAL SETUP

The studied structures are 7-nm-wide single GaN QWs grown by metal organic chemical vapor deposition along the (0001) axis. QWs are embedded in 45- or 140-nm $Al_{0.19}Ga_{0.81}N$ barriers grown on either sapphire (sample 1) or free-standing GaN (sample 2) substrates following the deposition of 3-μm-thick templates. The density of threading dislocations is of order of $(5–7) \times 10^8$ cm^{-2} in sample 1 and $< 5 \times 10^6$ cm^{-2} in sample 2. The schematic band diagram of the structure is given in Fig. 1(a). Because of the difference in spontaneous and piezoelectric polarizations between the well and barrier materials, interfacial fixed charges accumulate, resulting in a built-in electric field estimated as 1 MV/cm in this structure [30]. The built-in electric field pushes the electron and the hole toward opposite interfaces of the QW, breaking the symmetry of the excitonic wave function and inducing a permanent dipole moment along the growth axis. Optical excitation of the structure results in the screening of the built-in field, and in a blueshift E_{BS} of the exciton energy E_X with respect to E_0, the energy of the exciton ground state in the absence of photoexcitation [Fig. 1(b)]. The dependence of E_{BS} on the exciton density n is estimated by solving numerically the coupled Schrödinger-Poisson equations by the self-consistent procedure described in Ref. [30] and successfully used in our previous work [22]. The result of this calculation is nicely fitted by a linear law: $E_{BS} = \Phi_0 n$, where $\Phi_0 = 10^{-13}$ eV cm^2. This result is consistent with

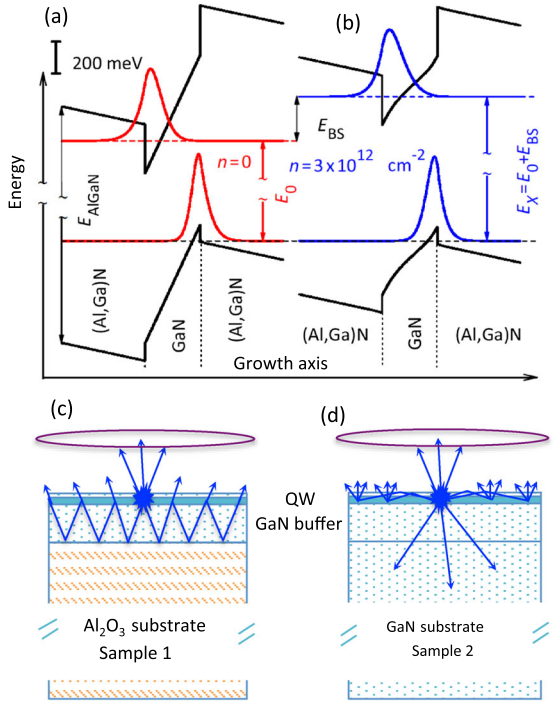

FIG. 1. Sketch of the band structure with typical electron and hole wave functions in the absence of photoexcitation (a) and under strong pumping corresponding to the exciton density of 3×10^{12} cm^{-2} (b); E_0 (E_X) is the exciton recombination energy in the zero- (high-) density limit; E_{BS} is the population-induced blueshift $E_{BS} = E_X - E_0 = n\Phi_0$. Measuring of E_{BS} provides an estimation of the exciton density. (c),(d) Schematic representation of the guiding effect in the structure grown on sapphire substrate (c) and reflection from the GaN/air interface in the structure grown on a GaN substrate (d).

the plate capacitor formula, which predicts linear dependence of the emission blueshift on the exciton density [34]. It can be applied in first approximation to our system, assuming that the correlation effects in the exciton gas are not too strong [35,36]. The energy of the unscreened QW (in the absence of photoexcited carriers) $E_0 \approx 3.0$ eV is obtained numerically and measured via time-resolved experiments presented below. Two types of experiments are performed on these structures: (i) spectrally and spatially resolved μPL measurements and (ii) spectrally and time-resolved PL measurements without spatial resolution. In μPL experiments, a continuous wave (cw) laser beam at $\lambda = 266$ nm is focused onto a 1-μm-diameter spot on the sample surface. In time-resolved measurements, excitons are photogenerated by a frequency-tripled Ti-sapphire laser at the same wavelength (pulse duration 150 fs, repetition rate 8 kHz, average power 660 nW) and using an approximately 100-μm excitation spot diameter. Spectrally resolved μPL images are obtained using a spectrometer equipped with a 150-gr/mm grating blazed at 390 nm. The detector for spatially resolved images is a CCD camera with 2048×512 pixels and pixel size of 13 μm, which corresponds to 0.4 μm on the sample

surface. Time-resolved measurements of the emission kinetics are performed using a Hamamatsu streak camera (model C10910 equipped with an S20 photocathode and UV coupling optics) enhanced for ultraviolet detection.

III. EXPERIMENTAL RESULTS AND DISCUSSION

A. Comparison between samples grown on sapphire and on GaN

Figure 2 shows μPL spectra (color encoded in log scale) as a function of the position in the sample plane along the x axis. The excitation spot position is at $x = 0$. The images are taken for the two samples and at four different temperatures (cw excitation power $P = 15$ mW). The excitonic recombination in the GaN template and/or substrate near $E = 3.48$ eV is rapidly quenched by increasing temperature. Below this energy, the emission is dominated by QW excitons with several phonon replicas below the zero-phonon line. At 30 K in both samples, one can clearly see the arrow-shaped pattern characteristic of exciton propagation accompanied by the decrease of the emission intensity and energy [22,23]. Similar patterns were observed in GaAs QWs at 2 K [5]. The spatial extension of the arrow-shaped pattern is twice larger in sample 2 (9 and 18 μm in sample 1 and sample 2, respectively). But in sample 1, this pattern is completely washed out at 300 K, while in sample 2, exciton emission and propagation persist up to room temperature. Room-temperature exciton transport in the GaN-grown sample is the main result that we discuss and model in this paper.

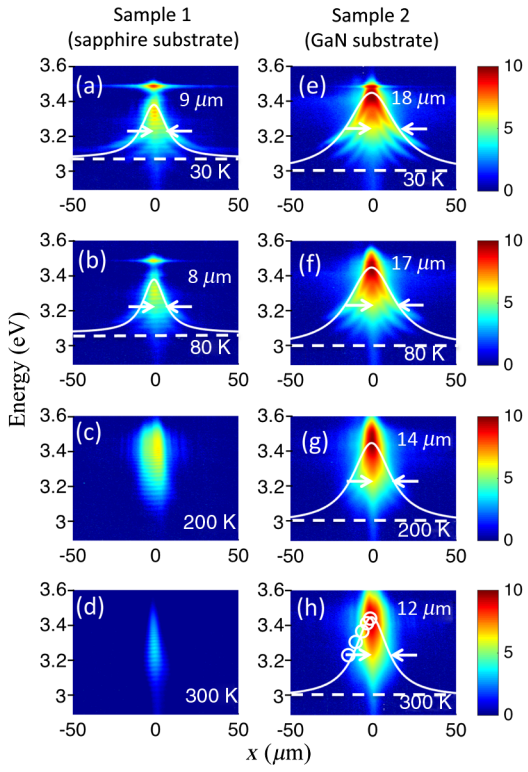

FIG. 2. μPL intensity (color encoded in log scale) at $T = 30$ (a,e), 80 (b,f), 200 (c,g), and 300 K (d,h) and cw excitation power $P = 15$ mW in sample 1 (a–d) and sample 2 (e–h). The abscissa shows the position along the x axis, with the origin at the spot position. The ordinate corresponds to the energy spectrum. Dashed lines indicate the energy of the QW exciton in the absence of the photoexcitation E_0 for each sample. Solid lines are Lorentzian profiles shown as a guide for the eye to describe the spatial profile of the energy distribution. Circles in (h) indicate the positions of the spectral maxima [cf. Fig. 5(d)].

Two prominent features can be observed in sample 1 only. These features are (1) interference fringes and (2) a strong emission tail with spatially independent energy at long distances (above 30 μm). Both features have already been observed in samples grown on sapphire substrates [22]. We attribute the fringes to Fabry-Perot interferences due to the reflection at the GaN/sapphire interface and the emission tails to the emission of excitons created by a secondary absorption process. Indeed, a significant part of the photons emitted around $r = 0$ by the QW itself is guided along the sample due to a high contrast between refractive indexes in GaN and sapphire, as well as in (Al,Ga)N and air. These photons are capable of creating, at larger distances, secondary excitons [Fig. 1(c)] or of scattering in the vertical direction. By contrast, in sample 2, interference fringes are suppressed, and the photon propagation is less efficient because it does not have a GaN/sapphire interface. Thus, sample 2 is more suitable for the accurate analysis of the exciton transport.

B. Exciton versus photon propagation

Despite the absence of the photon-guiding effect in sample 2, a nonzero density of photons is still propagating along the sample plane. The propagation of the photons remains possible, although less efficient than in sample 1, probably assisted by total internal reflection at the sample surface [Fig. 1(d)]. The effects related to photon propagation can be clearly seen in Figs. 3(a) and 3(b), where color encoded in logarithmic scale, spatial maps of μPL intensity normalized by the incident power are shown at 10 K for two different excitation powers. The color scale is the same as in Fig. 2, but the acquisition time is 10 times longer. An arrow-shaped pattern characteristic of exciton propagation and emission with density-dependent energy is accompanied by two bands of a weak emission far from the spot at approximately constant energy. We distinguish a broad emission band at 3.4 eV in Fig. 3(a) [3.2 eV in Fig. 3(b)] and the fluctuating energy tail at 3.05–3.1 eV, with a sudden jump of emission energy at $x \approx -30$ μm [Fig. 3(b)]. We argue that both emission bands are related to the scattering of the photons emitted at $x = 0$ and propagating in the QW plane. Indeed, the spectrum of this emission is broad, spreading down to 3 eV. The energy of its maximum is given by the initial ($x = 0$) blueshift of the exciton energy and, thus, depends on the incident power. The intensity of the scattered light at a given energy is proportional to the

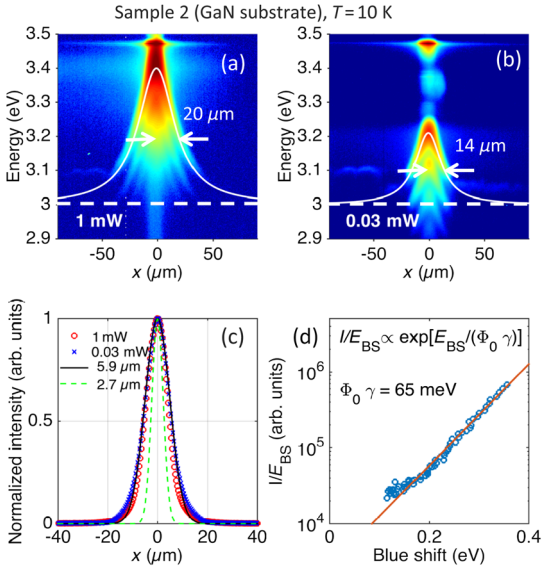

FIG. 3. Power dependence of the exciton transport in sample 2. (a),(b) Color maps of the logarithm of the PL intensity measured at 10 K for two different cw excitation powers. Color scale is the same as in Fig. 2. Dashed lines indicate the energy of the QW exciton in the absence of photoexcitation, $E_0 = 3$ eV. Solid lines are Lorentzians shown as a guide for the eye to describe the spatial profile of the energy distribution. (c) Intensity of PL (symbols) integrated from 2.85 to 3.47 eV as a function of position in the plane along the x axis for two different excitation powers. Green dashed line shows the emission profile at 3.48 eV (bulk GaN emission, close to the laser excitation profile). Black solid line is a Gaussian with HWHM $= 5.9$ μm. (d) The ratio between total emission intensity I and exciton energy blueshift E_{BS} (proportional to local exciton density $E_{\mathrm{BS}} = \Phi_0 n$) extracted from the μPL emission map shown in (a). Only the points within the arrow-shaped pattern are considered. Red solid line is a fit to the model described in the text.

product of the available photon density and the density of states in the QW. Thus, the two weak emission bands can be identified as scattered photons. The higher-energy broad emission band results from the peak in the photon density at $x = 0$; therefore, its energy depends on the power. The lower-energy fluctuating tail is related to the enhanced density of states at the energies corresponding to the localized exciton states in the QW. The jumps and fluctuations in this emission tail can be attributed to the disorder-induced potential fluctuations, which are not completely screened in this low-density regime ($n < 10^{11}$ cm^{-2}). The in-plane disorder can originate from both compositional disorder in the barriers and from monolayer fluctuations of the QW width. The characteristic energy scale U_d of this disorder potential is mainly determined by the strength of the built-in electric field. For our structures, we estimate $U_{\mathrm{rand}}^{\mathrm{1ML}} = 26$ meV per monolayer fluctuations and $U_{\mathrm{rand}}^{1\%} = 20$ meV per percent of aluminum content fluctuations. The excitons created far from the excitation spot contribute to the partial screening of this disorder potential and of the built-in electric field and, thus, can play an important role in the transport of excitons created directly under the laser spot [6,34,37].

C. Determination of the exciton energy and radiative lifetime in the zero-density regime

Because photon guiding is not fully suppressed in the absence of the GaN/sapphire interface, it is important to evaluate independently the energy E_0 of the exciton in the regime, where it is not affected by the photoexcitation [see Fig. 1(a)]. For this purpose, we perform time-resolved experiments using a pulsed laser excitation with low repetition frequency (much lower than the exciton recombination rate) and low average power. The excitation spot radius $R_0 = 50$ μm in these experiments is larger than the exciton propagation length so that the decay of the luminescence intensity can be attributed to the radiative recombination of excitons in the absence of the exciton transport. Typical time-resolved PL spectra measured in sample 2 at $T = 10$ K and at different time delays with respect to the excitation pulse are shown in Fig. 4(a). One can see that the QW emission energy E_X goes from 3.06 eV down to $E_0 \approx 3.0$ eV, the value that should, thus, be considered as the zero-density limit for the exciton energy in this sample. The integrated intensity of exciton emission as a function of time and the blueshift of the zero-phonon PL line with respect to E_0 are shown by symbols in Figs. 4(b) and 4(c), respectively. The blueshift exponentially decreases towards E_0 with a time constant of 2 μs corresponding to the effective exciton lifetime in the high-density regime, as shown by a solid line in Fig. 4(c). After the same time transient, the decay of the integrated intensity

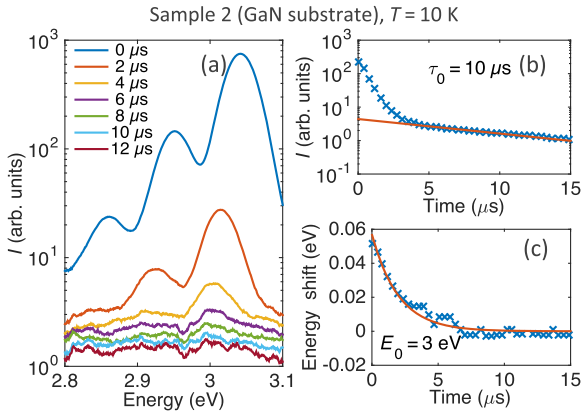

FIG. 4. Time-resolved exciton dynamics in sample 2 under large (100 μm diameter) excitation spot. (a) PL spectra measured at different time delays after the excitation pulse. (b) Exciton PL intensity (symbols) integrated in the energy range from 2.8 to 3.1 eV as a function of the time delay after the laser pulse. The solid line shows an exponential decay with characteristic time 10 μs. (c) Exciton energy shift (symbols) with respect to the lowest energy ($E_0 = 3$ eV), as a function of the time delay after the laser pulse. The solid line shows an exponential decay with characteristic time 2 μs.

reaches an exponential behavior with $\tau_0 = 10$ μs shown by a solid line in Fig. 4(b). This slow decay of the integrated intensity corresponding to almost constant emission energy E_0 provides the estimation of exciton radiative lifetime $\tau_0 = 10$ μs in the zero-density regime, where the screening of the built-in electric field is negligible. Similar analysis in sample 1 gives $\tau_0 = 22$ μs and $E_0 \approx 3.08$ eV. The reasons for this difference may be related to slight nonintentional variations in the QW width and in the barrier composition. From this analysis, we deduce that all the emission observed in cw experiments presented here stems from QW regions where the original built-in electric field and its fluctuations are partly screened due to photoexcitation, with exciton densities exceeding 10^{11} cm^{-2}.

D. Spatial extension of the exciton emission: Intensity versus blueshift pattern

On the basis of the above analysis, we can address exciton propagation quantitatively. Figure 3(c) shows the normalized integrated intensity of the QW exciton PL in sample 2 at $T = 10$ K and for the same excitation powers as in Figs. 3(a) and 3(b). The solid line is a fit to a Gaussian distribution with half width at half maximum HWHM $= 5.9$ μm, and the dashed line shows the laser intensity profile (measured at bulk GaN emission energy $E = 3.48$ eV) characterized by a twice smaller HWHM $= 2.7$ μm. It seems surprising at first sight that increasing the power does not help increase the intensity of the light emitted by excitons away from the excitation spot. To understand this effect, it is instructive to compare these spatial profiles of the exciton emission intensity with the corresponding spatial profiles of the emission energy that provide a direct measurement of the exciton density distribution. To do so, we plot (as a guide for the eye) on top of the color maps in Figs. 3(a) and 3(b), Lorentzian profiles with HWHM $= 20$ and 14 μm, respectively, which characterize the spatial distribution of the QW emission energy (even though the experimentally observed energy profiles have more complex shapes). One can see that the spatial extension of the energy distribution increases with power (by 30% when multiplying incident power by 30) and that it is wider than the corresponding intensity distribution, which is power independent [Fig. 3(c)]. The reason for this is the strong dependence of exciton radiative lifetime on the exciton density. Such dependence is a prominent feature of IXs: increasing exciton density reduces the exciton lifetime exponentially [22,30]. It can be clearly seen in spatially integrated time-resolved experiments presented above. As long as the exciton emission exhibits a measurable blueshift, the time dependence of the emission intensity cannot be described by a single-exponential decay [see Figs. 4(b) and 4(c)]. The relation between the exciton energy blueshift E_{BS} (proportional to local exciton density $E_{\mathrm{BS}} = \Phi_0 n$) and its radiative lifetime τ_{rad} can be directly extracted from the μPL emission maps by analyzing the ratio between the total emission intensity I and the exciton energy blueshift because $1/\tau_{\mathrm{rad}} \propto I/n \propto I/E_{\mathrm{BS}}$. An example of such analysis for the μPL map of Fig. 3(a) is shown in Fig. 3(d), where we consider only the points within the arrow-shaped pattern, where both exciton emission energy and intensity are well defined. One can clearly see an exponential behavior of I/E_{BS}. This behavior is consistent with the results of the numerical solution of the coupled Schrödinger-Poisson equations that predicts for this sample $\tau_{\mathrm{rad}} = \tau_0 \exp(-n/\gamma) = \tau_0 \exp(-E_{\mathrm{BS}}/\gamma\Phi_0)$, with $\gamma = 4.5 \times 10^{11}$ cm^{-2} [30]. By fitting this model to the data shown in Fig. 3(d) and using the value of $\Phi_0 = 10^{-13}$ eV cm^2 calculated from the same model, we get $\gamma = 6.5 \times 10^{11}$ cm^{-2}, not too far from the calculated value. A more detailed study of this phenomenon combining spatially and time-resolved μPL experiments will be of great interest, but it requires further experimental developments. Such studies are also mandatory to go further than our previous work [22] and other works [7,34,38,39] in the theoretical modeling of the exciton transport in this system involving strong disorder, dipolar interactions, and density-dependent exciton lifetimes. Here, we just wish to stress that the exciton propagation length is determined by the spatial profile of the emission energy blueshift rather than by the spatial profile of the integrated emission intensity.

E. Temperature dependence of the exciton transport: Role of the nonradiative losses

Let us now address the temperature dependence of the exciton transport and consider the spatial extension of the emission energy (and not the intensity) profiles that corresponds to the exciton density distribution across the sample plane. On top of the color maps in Fig. 2, we show as a guide for the eye the Lorentzian profiles characterizing the in-plane distribution of the exciton emission energy peak. The resulting values of the HWHM are indicated for each measurement, and they are far above the excitation spot size that was determined from the integration of the emission profile in the vicinity of the bulk GaN emission energy $E = 3.48 \pm 0.005$ eV. The energy corresponding to the zero-density limit (slightly different for the two samples as measured in time-resolved PL experiments at 10 K) is shown by the dashed lines. Here we neglect the combined effect of band-gap renormalization and the exciton localization on the zero-density emission energy. Strictly speaking, the variation of ± 25 meV can be expected [24]. This uncertainty defines the precision of the propagation length determination that we estimate to be of order of ± 3 μm.

At low temperature, the spatial profile of the emission energy is twice wider for sample 2 as compared to sample 1. The main reason for that is lower total density of excitons in sample 1, imposed by higher nonradiative losses. Indeed, the maximum blueshift at the excitation spot position is lower by approximately 70 meV in sample 1, which means that the total density is lower. This effect hinders exciton propagation because it is density activated, as can also be seen from the comparison of Figs. 3(a) and 3(b).

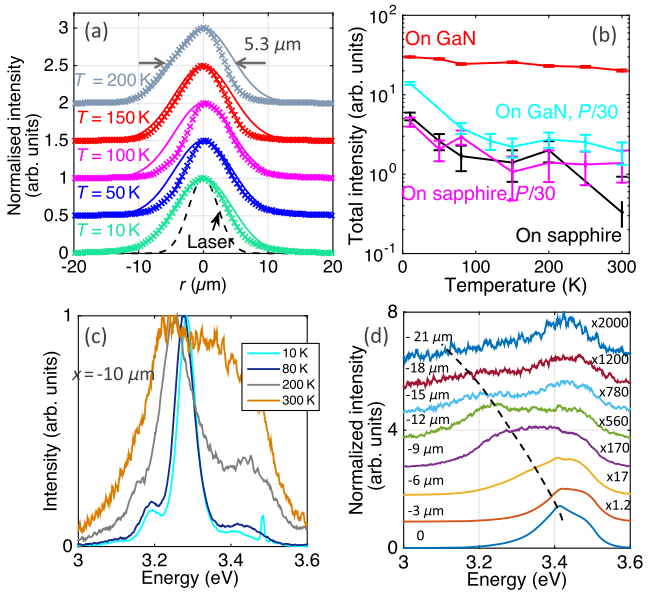

FIG. 5. Temperature dependence of the exciton transport. (a) Intensity of PL (symbols) in sample 2 (GaN substrate) integrated from 2.85 to 3.47 eV as a function of distance from the excitation spot, at five different temperatures. Solid lines are identical Gaussians with HWHM = 5.3 μm. Excitation power $P = 15$ mW. (b) PL intensity integrated over energy [same as in (a)] and over surface (from 0 to 100 μm from the spot) as a function of temperature for two different excitation powers [15 mW (red, black] and 0.5 mW (cyan, magenta) for the two samples. (c) Normalized PL spectra measured at four different temperatures at 10 μm distance from the excitation spot. (d) A set of spectra measured at room temperature in sample 2 at different distances from the excitation spot. Dashed line is a guide for the eye. The positions of the exciton emission peaks extracted from such spectra are also shown by white circles on top of the emission map in Fig. 2(h).

At room temperature, nonradiative recombination dominates in sample 1; therefore, the PL signal is too low to estimate the propagation length at 300 K [22].

In sample 2, the HWHM of the Lorentzian profile that defines the propagation length reaches 12 μm at room temperature. The corresponding set of spectra measured at room temperature in sample 2 at different distances from the excitation spot is shown in Fig. 5(d). The dashed line is a guide for the eye that mimics the evolution of the exciton emission energy with the distance. The positions of the exciton emission peaks are also shown by white circles on top of the emission map in Fig. 2(h).

Figure 5(a) shows a set of spectrally integrated and normalized spatial profiles of exciton emission in sample 2 for five different temperatures from 10 to 200 K. A constant vertical offset is introduced for clarity, and a dashed line shows the excitation spot profile characterized by a HWHM = 2.7 μm. By comparing the measured intensity profiles (symbols) with a Gaussian profile of HWHM = 5.3 μm and with the laser spot profile, we conclude that the exciton emission intensity pattern is twice more extended than the laser spot and that the temperature dependence of this extension is very weak. This means that with increasing temperature up to 200 K, excitons are not lost via nonradiative recombination but continue to contribute to the PL. This is in contrast with sample 1, where the nonradiative emission rate increases with the temperature. To quantify this effect, we compare in Fig. 5(b) the total emission intensity measured in experiments like those shown in Fig. 2 but integrated both in energy and in space over a surface of 8000 μm^2 for the two samples. One can see that at the highest excitation power in sample 2, the temperature dependence is, indeed, very weak, while in sample 1 the intensity decreases by almost one order of magnitude when increasing the temperature by a factor of 10. This means that the suppression of the nonradiative losses is crucial for exciton propagation at room temperature. At low excitation power, the total integrated PL intensity is similar for the two samples. Therefore, even in sample 2, nonradiative centers are not fully saturated in this weak excitation regime. The activation of nonradiative losses at low-power excitation is a well-known effect in GaN and (InGa)N heterostructures [40,41].

Despite low nonradiative losses and their weak temperature dependence, exciton emission maps for sample 2 at 30 and 300 K are very different [Figs. 2(e) and 2(h)]. The reason for this difference is the spectral broadening of the exciton line. This effect is illustrated in Fig. 5(c), where normalized exciton PL spectra measured 10 μm away from the laser spot are shown for four different temperatures. The peak emission energy is slightly different for the four spectra. This difference is related to the variation in the exciton density but may be contributed to by the renormalization of the band gap and the localization effects at low temperature [24,42,43]. At room temperature, the spectrum is so broad that even the first phonon replica cannot be distinguished. At low temperatures and low densities (far away from the excitation spot), the full linewidth at half maximum is $w_{10K} \approx 35 \pm 5$ meV, limited by the in-plane disorder stemming from monolayer fluctuations of the QW width and the fluctuations of the aluminum content in the barriers. Under the same conditions at room temperature, the line is so broad that it is quite difficult to estimate the linewidth precisely: $w_{300K} \approx 130 \pm 20$ meV. The increase of the exciton linewidth with the temperature has already been observed in GaN/(AlGa)N heterostructures [44]. It can be interpreted in terms of the coexistence of excitons with an electron-hole plasma. However, we expect a relatively large fraction of excitons in the QW. Indeed, efficient formation of radiative excitons from a high-density electron-hole plasma at room temperature has recently been demonstrated in similar structures [45]. For the highest cw excitation power used in this work ($P = 15$ mW) at $T = 10$ K the linewidth reaches 80 meV. The exciton emission profile remains Gaussian as long as the exciton

emission energy remains below $E = 3.4$ eV, corresponding to a blueshift $E_{BS} = 400$ meV. At higher carrier densities [reached only in the small area around the excitation spot at $P = 15$ mW; see Fig. 2(e)], the line shape changes and its width increases dramatically, as expected at Mott transition [44]. We estimate the corresponding Mott density from the emission blueshift $E_{BS} = 400$ meV as $n_{Mott} = 4 \times 10^{12}$ cm^{-2}, close to the values reported in Ref. [44].

IV. COMPARISON WITH THE MODELS

To go further in the understanding of the exciton transport and elucidate relevant mechanisms, we compare the above experimental results to the drift-diffusion models reported for indirect excitons in the literature [7,22,34,38,39]. Radial expansion of the optically created IX cloud due to dipolar repulsion between the excitons is usually described using the following nonlinear partial differential equation for exciton density n:

$$\partial n/\partial t = D\Delta n + \mu n \nabla(\Phi_0 n) - n/\tau + G. \quad (1)$$

Here, $G = (N_p/\pi R_0^2)\exp(-r^2/R_0^2)$ is the exciton density generation rate, N_p is the number of excitons generated per second, R_0 is the laser spot radius, τ is the recombination rate, D is the diffusion coefficient, and μ is the exciton mobility. The latter is related to the diffusion coefficient by the Einstein relation $\mu = D/(k_B T)$, where k_B is the Boltzman constant [46]. Eq. (1) is the most general form of the drift-diffusion equation. The first term on the right-hand side describes the diffusion and the second one describes the drift. For simplicity, we neglect exciton thermalization kinetics that can be important close to the excitation spot [39] and consider that exciton temperature is given by the lattice temperature. We also neglect non-radiative losses so that $\tau = \tau_{rad}$. This assumption is justified only in sample 2 under the highest-power excitation [see Fig. 5(b)]. The steady-state solutions $n(r)$ of Eq. (1) can be compared with the experimentally determined spatial profiles of the exciton emission energy, assuming $E_X = E_0 + E_{BS} = E_0 + \Phi_0 n$. The main difference between the different models available in the literature resides in the form of the diffusion coefficient and, therefore, the mobility that is directly related to the diffusion coefficient. We describe below three different approaches.

A. Model A: Exciton-exciton scattering

In the case of the free-exciton propagation at temperatures above the quantum degeneracy temperature, the exciton diffusion coefficient is given by the exciton-exciton scattering and depends on both temperature and density $D_0 \propto T/n$. However, free-exciton propagation can also be hindered by disorder. In Ref. [34], exciton transport in the presence of a localizing disorder is considered by taking into account the ability of excitons to screen the disorder potential (thermionic model). As a result, the diffusion coefficient is both temperature and density dependent in such a way that when excitons are localized at $\Phi_0 n + k_B T < U_{rand}$, where U_{rand} is the amplitude of the disorder potential, the diffusion is reduced with respect to D_0. This approach yields

$$D \propto \alpha \frac{T}{n} \exp\left(\frac{-U_{rand}}{\Phi_0 n + k_B T}\right), \quad (2)$$

where $\alpha = [4/(\hbar\pi)](a_B/2d)^2(M_r/M)^2$, a_B is the exciton Bohr radius, M (M_r) is the total (reduced) mass of the excitons, and d is the length of the excitonic dipole.

B. Model B: Localizing disorder

A similar thermionic form of the density and temperature-activated diffusion coefficient but ignoring exciton-exciton scattering ($D_0 = \text{const}$) has been proven to be very successful and efficient to describe exciton transport in GaAs/(Ga, Al)As coupled QWs [7,39]. In this case, the diffusion coefficient reads

$$D = D_0 \exp\left(\frac{-U_{rand}}{\Phi_0 n + k_B T}\right). \quad (3)$$

C. Model C: Randomly distributed scatterers

Rapaport *et al.* [38] used another approach to describe the effect of the disorder-induced exciton scattering. They assumed that the interface roughness can be described by a random distribution of quasielastic, hard-sphere scattering centers, with a characteristic distance l between them. In this case, and in the limit of strong disorder (relevant even for the best GaAs-based QWs), the diffusion coefficient can be expressed as $D = l v_{th}$, where $v_{th} = \sqrt{2k_B T/M}$ is the thermal velocity.

D. Comparison between the models and the data

We apply these three models to our system, taking into account the exponential dependence of the radiative lifetime on the density, which is specific of polar heterostructures. The corresponding parameters τ_0 and γ are measured independently, as described above. Other parameters are chosen to ensure the best fit of the experimental data: $U_{rand} = 0.03$ eV, $D_0 = 1$ cm^2/s, $l = 3$ nm, $N_p = k \times 10^{14}$ s^{-1}, where $k = 1.2$, 1.8, 1.5, 1.2 in Figs. 6(a)–6(d), respectively. Exciton mass in GaN is $M = 1.2 m_0$, where m_0 is a free-electron mass, $R_0 = 2\mu$m, and $\alpha = 1.5 \times 10^8$ cm^2/s. The result is shown in Fig. 6. The dashed lines show the Lorentzian profiles of the exciton blueshift patterns measured at four different temperatures, similar to those shown by white lines in Figs. 2(e)–2(h), but here the measurements at $P = 5$ mW are analyzed. For each temperature, only the experimentally observed part of the Lorentzian is shown, corresponding to

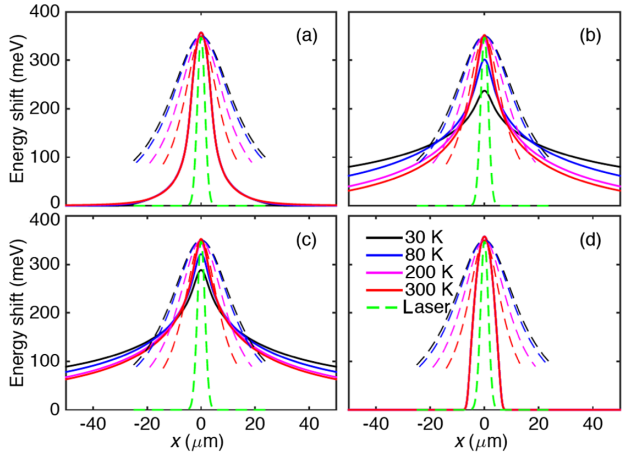

FIG. 6. Modeling of the exciton propagation. The dashed lines are Lorentzian profiles that characterize experimentally measured blueshifts of the exciton energy as a function of position with respect to the excitation spot at different temperatures and at $P = 5$ mW. The solid lines with the same color code are results of the calculations within the models A (a), B (b), and C (c) described in the text and without diffusion ($D = 0$) (d). The green dashed lines represent the excitation density profile used in the calculations.

the arrow-shaped pattern. The solid lines are calculated within the three models [Figs. 6(a)–6(c)], and also in the absence of diffusion, assuming $D = 0$ [Fig. 6(d)]. Because the relation between the blueshift of the exciton emission energy and its integrated intensity is extracted from the experiment, it is sufficient to reproduce numerically the emission energy profile to get the correct intensity profile from the model, at least within the arrow-shaped pattern.

The first conclusion that can be drawn from this analysis is that even in the absence of diffusion, the density-dependent recombination rate leads to the broadening of the exciton cloud with respect to the excitation spot [Fig. 6(d)]. However, this effect is small and cannot account for the experimentally measured profiles of the blueshift. Therefore, the broadening of the exciton density profile is definitively a consequence of the diffusion and drift of the excitons. This conclusion is valid from $T = 10$ K up to room temperature. The second conclusion concerns the mechanisms of the exciton diffusion. One can see in Figs. 6(a) and 6(b) that both exciton-exciton scattering and localizing disorder models show a striking difference with the experiments. Indeed, in the framework of the exciton-exciton scattering model (model A), the high exciton density required us to ensure a significant energy shift E_{BS} completely inhibits the diffusion, because in this case, $D \propto 1/n$ [see Eq. (2)]. On the other hand, the localizing disorder model (model B) implies very strong temperature dependence. Indeed, at high exciton densities, the disorder potential is completely screened. In this regime, $D = D_0$, and $\mu \propto 1/T$. The drift current being dominant at $E_{\mathrm{BS}} \gg k_B T$ results in very efficient suppression of the exciton drift when the temperature is increased. Such quenching of the exciton transport is not observed experimentally. Thus, it appears that the randomly distributed scatterers model (model C) provides the best (albeit, not perfect) description of our experiments. Remarkably, because $E_{\mathrm{BS}} \gg k_B T$ up to room temperature all across the arrow-shaped pattern, we can claim that exciton transport in this regime is rather controlled by the exciton drift (due to dipolar repulsion) and not by diffusion like in the case of traditional nondipolar excitons or photoexcited electron-hole plasma [47,48]. This conclusion, however, is valid only in the cw excitation regime, where a significant density of excitons is present along the QW plane across all the experimentally achievable range of distances from the excitation spot.

V. CONCLUSIONS

We demonstrate exciton transport in a GaN/(Al, Ga)N QWs and measure propagation lengths up to 12 μm at room temperature and up to 20 μm at 10 K. The comparison of spatial and time-resolved experiments provides clear evidence that exciton transport is accompanied by photon propagation along the structure plane. This photon propagation is much stronger in samples grown on sapphire but, nevertheless, cannot be neglected in GaN-grown samples. It is responsible for the partial screening of the built-in electric field so that the zero-density regime is hard to reach in cw experiments.

From the comparison of two nominally identical samples grown on GaN and sapphire, respectively, we conclude that the drastic reduction of nonradiative losses at room temperature in the sample grown on GaN substrate is the key element to achieve room-temperature exciton transport. In this sample, the radiative efficiency is nearly temperature independent. Such a remarkable quality allows us to study exciton transport from 10 to 300 K and to compare the results with the theoretical predictions of several available models. It appears that under cw excitation conditions, the thermally activated scattering on the point defects is most probably the main mechanism that limits exciton propagation. Therefore, further optimization of the interface quality in the QWs should help increase exciton transport lengths. We also show that even at room temperature, exciton transport is dominated by the drift current rather than by the diffusion current. Extended studies of the exciton transport temperature dependence were not possible in the previous works, either because of exciton dissociation in GaAs coupled QWs [8,11,13] or because of dominant nonradiative losses in wide-band-gap polar QWs grown on sapphire substrates [22,23]. Our results provide not only a rich playground for further understanding of exciton transport and elaboration of new transport models in order to optimize exciton propagation but also a material basis for the development of room-temperature excitonic devices for optical signal processing.

ACKNOWLEDGMENTS

We are grateful to D. Scalbert and L. V. Butov for enlightening discussions. This work is supported by the European Union (PITN-GA-2011-289968 INDEX) and French National Research Agency (ANR-15-CE30-0020-02 OBELIX).

[1] H. J. Polland, L. Schultheis, J. Kuhl, E. O. Göbel, and C. W. Tu, Lifetime Enhancement of Two-Dimensional Excitons by the Quantum-Confined Stark Effect, Phys. Rev. Lett. **55**, 2610 (1985).

[2] Y. J. Chen, Emil S. Koteles, B. S. Elman, and C. A. Armiento, Effect of electric fields on excitons in a coupled double-quantum-well structure, Phys. Rev. B **36**, 4562 (1987).

[3] A. Alexandrou, J. A. Kash, E. E. Mendez, M. Zachau, J. M. Hong, T. Fukuzawa, and Y. Hase, Electric-field effects on exciton lifetimes in symmetric coupled $GaAs/Al_xGa_{1-x}As$ double quantum wells, Phys. Rev. B **42**, 9225 (1990).

[4] L. V. Butov, A. A. Shashkin, V. T. Dolgopolov, K. L. Campman, and A. C. Gossard, Magneto-optics of the spatially separated electron and hole layers in $GaAs/Al_xGa_{1-x}As$ coupled quantum wells, Phys. Rev. B **60**, 8753 (1999).

[5] Z. Vörös, R. Balili, D. W. Snoke, L. Pfeiffer, and K. West, Long-Distance Diffusion of Excitons in Double Quantum Well Structures, Phys. Rev. Lett. **94**, 226401 (2005).

[6] M. Remeika, J. C. Graves, A. T. Hammack, A. D. Meyertholen, M. M. Fogler, L. V. Butov, M. Hanson, and A. C. Gossard, Localization-Delocalization Transition of Indirect Excitons in Lateral Electrostatic Lattices, Phys. Rev. Lett. **102**, 186803 (2009).

[7] J. R. Leonard, M. Remeika, M. K. Chu, Y. Y. Kuznetsova, A. A. High, L. V. Butov, J. Wilkes, M. Hanson, and A. C. Gossard, Transport of indirect excitons in a potential energy gradient, Appl. Phys. Lett. **100**, 231106 (2012).

[8] G. Grosso, J. Graves, A. T. Hammack, A. A. High, L. V. Butov, M. Hanson, and A. C. Gossard, Excitonic switches operating at around 100 K, Nat. Photonics **3**, 577 (2009).

[9] A. A. High, A. T. Hammack, L. V. Butov, M. Hanson, and A. C. Gossard, Exciton optoelectronic transistor, Opt. Lett. **32**, 2466 (2007).

[10] Y. Y. Kuznetsova, M. Remeika, A. A. High, A. T. Hammack, L. V. Butov, M. Hanson, and A. C. Gossard, All-optical excitonic transistor, Opt. Lett. **35**, 1587 (2010).

[11] P. Andreakou, S. V. Poltavtsev, J. R. Leonard, E. V. Calman, M. Remeika, Y. Y. Kuznetsova, L. V. Butov, J. Wilkes, M. Hanson, and A. C. Gossard, Optically controlled excitonic transistor, Appl. Phys. Lett. **104**, 091101 (2014).

[12] Alexander G. Winbow, Aaron T. Hammack, Leonid V. Butov, and Arthur C. Gossard, Photon storage with nanosecond switching in coupled quantum well nanostructures, Nano Lett. **7**, 1349 (2007).

[13] Alex A. High, Ekaterina E. Novitskaya, Leonid V. Butov, Micah Hanson, and Arthur C. Gossard, Control of exciton fluxes in an excitonic integrated circuit, Science **321**, 229 (2008).

[14] S. Lazić, A. Violante, K. Cohen, R. Hey, Ronen Rapaport, and P. V. Santos, Scalable interconnections for remote indirect exciton systems based on acoustic transport, Phys. Rev. B **89**, 085313 (2014).

[15] Charles-Edouard Bardyn, Torsten Karzig, Gil Refael, and Timothy C. H. Liew, Topological polaritons and excitons in garden-variety systems, Phys. Rev. B **91**, 161413 (2015).

[16] Marc Baldo and Vladimir Stojanović, Optical switching: Excitonic interconnects, Nat. Photonics **3**, 558 (2009).

[17] L. V. Butov and A. I. Filin, Energy relaxation and transport of indirect excitons in AlAs/GaAs coupled quantum wells in magnetic fields, Zh. Eksp. Teor. Fiz. **114**, 1115 (1998) [JETP **87**, 608 (1998)].

[18] Kobi Cohen, Ronen Rapaport, and Paulo V. Santos, Remote Dipolar Interactions for Objective Density Calibration and Flow Control of Excitonic Fluids, Phys. Rev. Lett. **106**, 126402 (2011).

[19] M. Alloing, A. Lemaître, and F. Dubin, Quantum signature blurred by disorder in indirect exciton gases, Europhys. Lett. **93**, 17007 (2011).

[20] A. Gärtner, A. W. Holleitner, J. P. Kotthaus, and D. Schuh, Drift mobility of long-living excitons in coupled GaAs quantum wells, Appl. Phys. Lett. **89**, 052108 (2006).

[21] A. Violante, K. Cohen, S. Lazić, R. Hey, R. Rapaport, and P. V. Santos, Dynamics of indirect exciton transport by moving acoustic fields, New J. Phys. **16**, 033035 (2014).

[22] F. Fedichkin, P. Andreakou, B. Jouault, M. Vladimirova, T. Guillet, C. Brimont, P. Valvin, T. Bretagnon, A. Dussaigne, N. Grandjean, and P. Lefebvre, Transport of dipolar excitons in (Al, Ga)N/GaN quantum wells, Phys. Rev. B **91**, 205424 (2015).

[23] Y. Y. Kuznetsova, F. Fedichkin, P. Andreakou, E. V. Calman, L. V. Butov, P. Lefebvre, T. Bretagnon, T. Guillet, M. Vladimirova, C. Morhain, and J. M. Chauveau, Transport of indirect excitons in ZnO quantum wells, Opt. Lett. **40**, 3667 (2015).

[24] M. Leroux, N. Grandjean, M. Laügt, J. Massies, B. Gil, P. Lefebvre, and P. Bigenwald, Quantum confined Stark effect due to built-in internal polarization fields in (Al, Ga)N/GaN quantum wells, Phys. Rev. B **58**, R13371 (1998).

[25] M. Esmaeili, M. Gholami, H. Haratizadeh, B. Monemar, P. Holtz, S. Kamiyama, H. Amano, and I. Akasaki, Experimental and theoretical investigations of optical properties of GaN/AlGaN MQW nanostructures. Impact of built-in polarization fields, Opto-Electron. Rev. **17**, 293 (2009).

[26] C. Morhain, T. Bretagnon, P. Lefebvre, X. Tang, P. Valvin, T. Guillet, B. Gil, T. Taliercio, M. Teisseire-Doninelli, B. Vinter, and C. Deparis, Internal electric field in wurtzite $ZnO/Zn_{0.78}Mg_{0.22}O$ quantum wells, Phys. Rev. B **72**, 241305 (2005).

[27] P. Bigenwald, P. Lefebvre, T. Bretagnon, and B. Gil, Confined excitons in GaN/AlGaN quantum wells, Phys. Status Solidi (b) **216**, 371 (1999).

[28] A. A. High, J. R. Leonard, A. T. Hammack, M. M. Fogler, L. V. Butov, A. V. Kavokin, K. L. Campman, and A. C. Gossard, Spontaneous coherence in a cold exciton gas, Nature (London) **483**, 584 (2012).

[29] Mathieu Alloing, Mussie Beian, Maciej Lewenstein, David Fuster, Yolanda González, Luisa González, Roland Combescot, Monique Combescot, and François Dubin,

Evidence for a Bose-Einstein condensate of excitons, Europhys. Lett. **107**, 10012 (2013).

[30] P. Lefebvre, S. Kalliakos, T. Bretagnon, P. Valvin, T. Taliercio, B. Gil, N. Grandjean, and J. Massies, Observation and modeling of the time-dependent descreening of internal electric field in a wurtzite $GaN/Al_{0.15}Ga_{0.85}N$ quantum well after high photoexcitation, Phys. Rev. B **69**, 035307 (2004).

[31] J. C. Harris, T. Someya, S. Kako, K. Hoshino, and Y. Arakawa, Time-resolved photoluminescence of $GaN/Al_{0.5}Ga_{0.5}N$ quantum wells, Appl. Phys. Lett. **77**, 1005 (2000).

[32] F. Natali, D. Byrne, M. Leroux, B. Damilano, F. Semond, A. Le Louarn, S. Vezian, N. Grandjean, and J. Massies, Inhomogeneous broadening of $Al_xGa_{1-x}N/GaN$ quantum wells, Phys. Rev. B **71**, 075311 (2005).

[33] T. Paskova, D. A. Hanser, and K. R. Evans, GaN substrates for III-nitride devices, Proc. IEEE **98**, 1324 (2010).

[34] A. L. Ivanov, Quantum diffusion of dipole-oriented indirect excitons in coupled quantum wells, Europhys. Lett. **59**, 586 (2002).

[35] B. Laikhtman and R. Rapaport, Correlations in a two-dimensional Bose gas with long-range interaction, Europhys. Lett. **87**, 27010 (2009).

[36] Christoph Schindler and Roland Zimmermann, Analysis of the exciton-exciton interaction in semiconductor quantum wells, Phys. Rev. B **78**, 045313 (2008).

[37] M. Remeika, J. R. Leonard, C. J. Dorow, M. M. Fogler, L. V. Butov, M. Hanson, and A. C. Gossard, Measurement of exciton correlations using electrostatic lattices, Phys. Rev. B **92**, 115311 (2015).

[38] Ronen Rapaport, Gang Chen, and Steven H. Simon, Nonlinear dynamics of a dense two-dimensional dipolar exciton gas, Phys. Rev. B **73**, 033319 (2006).

[39] A. T. Hammack, L. V. Butov, J. Wilkes, L. Mouchliadis, E. A. Muljarov, A. L. Ivanov, and A. C. Gossard, Kinetics of the inner ring in the exciton emission pattern in coupled GaAs quantum wells, Phys. Rev. B **80**, 155331 (2009).

[40] Satoshi Watanabe, Norihide Yamada, Masakazu Nagashima, Yusuke Ueki, Chiharu Sasaki, Yoichi Yamada, Tsunemasa Taguchi, Kazuyuki Tadatomo, Hiroaki Okagawa, and Hiromitsu Kudo, Internal quantum efficiency of highly-efficient $In_xGa_{1-x}N$-based near-ultraviolet light-emitting diodes, Appl. Phys. Lett. **83**, 4906 (2003).

[41] J. Mickevičius, G. Tamulaitis, M. Shur, M. Shatalov, J. Yang, and R. Gaska, Internal quantum efficiency in AlGaN with strong carrier localization, Appl. Phys. Lett. **101**, 211902 (2012).

[42] Y. P. Varshni, Temperature dependence of the energy gap in semiconductors, Physica (Utrecht) **34**, 149 (1967).

[43] Annamraju Kasi Viswanath, Joo In Lee, C. R. Lee, J. Y. Leem, and Dongho Kim, Free exciton transitions and Varshni's coefficients for GaN epitaxial layers grown by horizontal lp-mocvd, Solid State Commun. **108**, 483 (1998).

[44] G. Rossbach, J. Levrat, G. Jacopin, M. Shahmohammadi, J.-F. Carlin, J.-D. Ganière, R. Butté, B. Deveaud, and N. Grandjean, High-temperature Mott transition in wide-band-gap semiconductor quantum wells, Phys. Rev. B **90**, 201308 (2014).

[45] Andreas Hangleiter, Zuanming Jin, Marina Gerhard, Dimitry Kalincev, Torsten Langer, Heiko Bremers, Uwe Rossow, Martin Koch, Mischa Bonn, and Dmitry Turchinovich, Efficient formation of excitons in a dense electron-hole plasma at room temperature, Phys. Rev. B **92**, 241305 (2015).

[46] We assume that the system is far from quantum degeneracy $T > T_{\mathrm{dB}}$, where T_{dB} is the de Broigle temperature of the quantum degeneracy, and neglect quantum form of the Einstein relation $\mu = D/(k_B T_{\mathrm{dB}}) \exp(T_{\mathrm{dB}}/T - 1)$ [34].

[47] M. A. Tamor and J. P. Wolfe, Drift and Diffusion of Free Excitons in Si, Phys. Rev. Lett. **44**, 1703 (1980).

[48] K. T. Tsen, O. F. Sankey, G. Halama, Shu-Chen Y. Tsen, and H. Morkoc, Transport of the photoexcited electron-hole plasma in GaAs quantum wells, Phys. Rev. B **39**, 6276 (1989).